Applied Ocean Research 109 (2021) 102557

Contents lists available at ScienceDirect

Applied Ocean Research

journal homepage: www.elsevier.com/locate/apor

Near real-time calculation of submarine fault properties using an inverse model of acoustic signals

Bernabe Gomez *, Usama Kadri

School of Mathematics, Cardiff University, Senghennydd road, Cardiff CF24 4AG, UK

ARTICLE INFO

Keywords:
Inverse solution
Acoustic radiation

ABSTRACT

A submarine earthquake that generates a tsunami sends a family of acoustic signals that carry information on the fault dynamics and geometry. These signals travel at the speed of sound in water, much greater than the phase speed of the gravity waves, and thus can act as early warning of tsunamis. To utilise this property in real-time, a semi-analytical inverse approach is employed assuming the fault is slender and the water depth is constant, allowing the calculation of some fault parameters analytically. However, the remaining parameters require a numerical evaluation, which increases the calculation time substantially. In order to overcome this difficulty, a probabilistic inverse model is proposed. The model analyses data at the envelope of a pressure signal, which reduces numerical complexities. More specifically, it selects multiple measurement points, in order to produce several sets of solutions within given ranges of the properties. The model is applied to real hydrophone recordings, where the fault geometry and dynamics are estimated near real-time on a standard PC. Some aspects of the model are general and can be used to estimate simplified geometry and dynamics of various signal sources from violent events in the ocean, such as impacting meteorites, submarine explosions, landslides and rogue waves.

1. Introduction

A tsunami is a series of surface water waves that are generated in the ocean, sea or lake as a response to a sudden vertical displacement of a large volume of water. It is often caused by a violent geophysical event such as a submarine earthquake, a landslide or a submarine explosion. The sudden vertical motion is associated with a slight compression of the water layer that affects the properties of the generated tsunami (Abdolali et al., 2019; Nosov, 1999). In addition, it generates compression-type waves, known as acoustic-gravity waves (Yamamoto, 1982), that travel at the speed of sound in water, $c \simeq 1500\ \mathrm{ms}^{-1}$, which far exceeds the maximum tsunami phase speed. For example, in a water layer of depth $h = 2000$ m, a tsunami would propagate at a speed that is more than 10 times slower than the phase speed of acoustic-gravity waves. Hence, acoustic-gravity waves can be used for early warning as originally noted by Yamamoto (1982). It is believed that acoustic-gravity waves can leave measurable bottom pressure signals far from the fault (Kadri and Stiassnie, 2012; Stiassnie, 2010), which allows them to be recorded by distant hydrophones (Okal, 2001) providing insight into frequency components of both the tsunami and the acoustic-gravity waves even at the low end of the spectrum (Okal et al., 2007).

Hendin and Stiassnie (2013) developed a standard inverse approach capable of retrieving some of the source characteristics from pressure recordings by employing a piston model with cylindrical geometry and a three-dimensional integral description of the pressure field. However, such model requires extensive computations and applying it in early warning systems is rather challenging. To overcome this difficulty, Mei and Kadri (2018) employed slender body theory to derive a closed form analytical solution of the 3D pressure field, which is essential for near real-time inverse calculations. The model implies several simplifications: (1) gravity effects were neglected since gravity and acoustic modes are virtually decoupled after a long propagation distance (see Mei and Kadri, 2018 and references within); (2) the fault is assumed to be slender with width $2b$ and length $2L$ (see Fig. 1), which is a reasonable assumption as illustrated in Table 1 of Ref. Mei and Kadri (2018); (3) the fault moves vertically upwards with a constant speed (W_0) for a time duration ($2T$); (4) the water depth h is constant, which is a fine assumption as long as the characteristic lengthscales of the sea bed topography are several orders of magnitude smaller than the water

* Corresponding author.
E-mail addresses: gomezperezb@cardiff.ac.uk (B. Gomez), kadriu@cardiff.ac.uk (U. Kadri).

https://doi.org/10.1016/j.apor.2021.102557
Received 10 September 2020; Received in revised form 19 January 2021; Accepted 21 January 2021
Available online 14 February 2021

depth (i.e. in deep ocean far from deep tranches or shelf breaks) - this has been recently validated numerically by Williams et al. (2021); (5) the sea floor is rigid, which is a fine assumption as long as the water layer is deep enough for the analysed acoustic mode, otherwise the phase speed of the mode will change dramatically and the elasticity of the sea floor will need to be considered as illustrated in Fig. 2a of Ref. Eyov et al. (2013).

In this study we develop a probabilistic inverse model based on the slender fault solution (Mei and Kadri, 2018). Since the model is based on an analytical solution comprising trigonometric functions, some properties may have multiple solutions that are out of the usual range. To avoid such solutions, we confine the range of the fault properties following the literature. As a range guideline, we consider the fault approximations by Bilek and Lay (1999); Krüger and Ohrnberger (2005), which can be correlated with the pressure signal (Cecioni and Bellotti, 2018), and the moment of magnitude of the event (Wells and Coppersmith, 1994). It is worth noting that, the slender fault geometry and the dynamics considered here are not a simplification of the earthquake dynamics itself, but rather represent an effective vertical motion caused by the much more complicated rupture dynamics. Thus, the horizontal component of the rupture is ignored, e.g. while a rupture can last, say, for tens of minutes, the effective uplift we consider here may only have a duration of a few seconds. Note that effective rupture properties for tsunami generation have been studied extensively, in particular major submarine earthquakes. For example, the rupture length in the case of the 26 December 2004 Sumatra earthquake is 900 km long (Fujii and Satake, 2007); the effective surface vertical uplift of the 22 May 1960 Chile earthquake is 2 m (Moreno et al., 2009); and the effective vertical uplift of the Maule 27 February 2010 Chile earthquake is 3–5 m and its width is 20–50 km (Maksymowicz et al., 2017).

A brief background on the slender fault analytical solution is given in Section 2 (further details can be found in Ref. Mei and Kadri, 2018). The inverse model is described step by step in Section 3 using both synthetic and real examples. A sensitivity analysis is carried out in Section 4, and analysis of synthetic and real data are then presented in Section 5. Finally, the discussion and conclusions are drawn in Section 6.

2. Background

2.1. Acoustic radiation from slender fault: analytical solution

The propagation of acoustic-gravity waves in a slightly compressible fluid is governed by the three dimensional wave equation Stiassnie (2010)

$$\frac{\partial^2\phi}{\partial x^2}+\frac{\partial^2\phi}{\partial y^2}+\frac{\partial^2\phi}{\partial z^2}=\frac{1}{c^2}\frac{\partial^2\phi}{\partial t^2}, \tag{1}$$

where ϕ is the velocity potential, the velocity field is defined by $\mathbf{u}=\nabla\phi$ and c is the speed of sound in water (1500 m/s). Since gravity effects are neglected, at the free surface ($z=h$), the pressure is assumed to be uniform and zero

Table 1
Input ranges of source characteristics for the inverse model, based on Wells and Coppersmith (1994).

Property	Range
Length [km]	1–100
Width [km]	1–50
Duration [s]	0–15
Uplift speed [m/s]	0.005–0.500

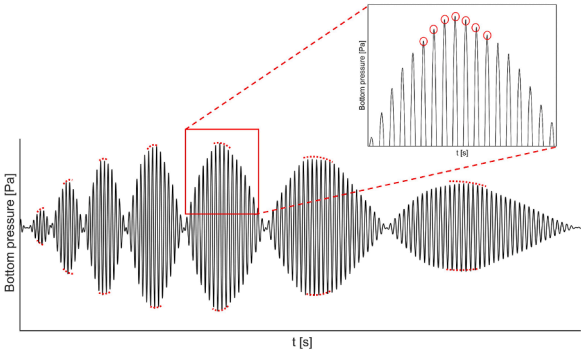

Fig. 2. Synthetic sound signal from an slender fault. Points that meet the condition $\sin(kb)=1$ are highlighted in red.

$$\phi=0 \quad \text{at} \quad z=h, \tag{2}$$

and thus we can confine our analysis to pure acoustic signals, neglecting effects of gravity. On the seabed, located at $z=0$, a piston model simulates the vertical displacement of the fault by

$$\frac{\partial\phi}{\partial z}=\begin{cases} W_0\tau(t) & |x|<b,\ |y|<L \\ 0 & \text{elsewhere}\end{cases}, \qquad \tau(t)=\begin{cases}1 & -T<t<T \\ 0 & |t|>T\end{cases}. \tag{3}$$

Multiple scale coordinates are introduced, $x, z, X=\epsilon^2 x, Y=\epsilon y$, where $\epsilon=b/L\ll 1$ is the slenderness parameter. The solution of Eq. (1), with the boundary conditions (2) and (3) is derived by a double Fourier transform, followed by the corresponding double inverse Fourier transform which results in a countable infinity of acoustic modes. The first acoustic modes are progressive, followed by evanescent modes that decay exponentially with distance. For the sake of brevity, we consider the leading (first) progressive mode only, which contains most of the energy (Mei and Kadri, 2018). Moreover, we are interested in bottom pressure signatures that are recorded sufficiently far from the fault, at distances in the range of hundreds to a few thousands of kilometres, to avoid the contribution of both evanescent and surge modes (see Eq. (38) of Ref.Yamamoto (1982)). Note that the water density, ρ, is assumed to be constant so that the SOFAR (Sound Fixing and Ranging) channel is not considered here. Nevertheless, it is important to note that the leading mode frequency is extremely low, thus, the whole water depth

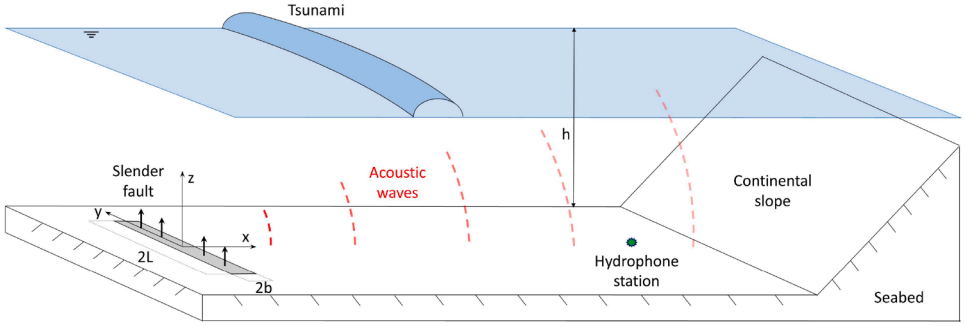

Fig. 1. Generation of tsunami and acoustic waves by an uplifting slender fault, leaving measurable pressure signals at distant locations.

serves as a wave-guide (Stiassnie, 2010), such that it cannot be trapped in the SOFAR channel even if water density variations were taken into account. Finally, applying a stationary phase approximation the bottom pressure is derived (see Ref. (Mei and Kadri, 2018)),

$$p = \rho W_0 |A| \frac{2^{5/2} c^3 t^{1/2}}{h\pi^{1/2}\omega^{3/2} x_0} \left[1-(x_0/ct)^2\right]^{1/4} \sin\left(\frac{\omega}{c}\frac{x_0/ct}{\sqrt{1-(x_0/ct)^2}} b\right) \times \sin\left(\frac{\omega}{\sqrt{1-(x_0/ct)^2}} T\right) \cos\left(kx_0 - \Omega t - \frac{\pi}{4}\right), \tag{4}$$

where (x_0, y_0) is the epicentre coordinates of the fault relative to the point where the pressure is computed (or measured), k is the wavenumber, Ω is the frequency of the pressure signal and ω is the frequency associated with the first mode,

$$\omega = \frac{\pi c}{2h}; \tag{5}$$

and $A(K, X, Y)$ is the two dimensional envelope given by

$$A = \frac{1-\mathrm{i}}{2}\left(C\left(\sqrt{\frac{K}{\pi X}}(\epsilon L + Y)\right) + C\left(\sqrt{\frac{K}{\pi X}}(\epsilon L - Y)\right)\right) + \frac{1+\mathrm{i}}{2}\left(S\left(\sqrt{\frac{K}{\pi X}}(\epsilon L + Y)\right) + S\left(\sqrt{\frac{K}{\pi X}}(\epsilon L - Y)\right)\right), \tag{6}$$

with Fresnel cosine and sine integrals denoted as C and S, with the frequency and wavenumber (Mei and Kadri, 2018),

$$k(\Omega) \equiv K = \frac{x}{c^2 t}\Omega, \quad \Omega = \frac{\omega}{\sqrt{1-(x/ct)^2}}. \tag{7}$$

Note that we are interested in signals measured briefly after the critical arrival time ($t_{cr} = x/c$). This helps avoiding reverberations (that arrive at a later time) when analysing real signals.

2.2. Inverse solution for acoustic radiation from a slender fault

We consider an arbitrary slender fault eruption to create a numerical synthetic pressure signal of the leading acoustic mode using Eq. (4). The signal can be considered as a recorded pressure signal. The inverse model is then applied in order to retrieve the properties of the eruption, hence the slender fault geometry and dynamics. Initially, the fault location (x_0, y_0) and eruption time (t_0) are calculated using Eqs. (8.2) and (8.3) of Ref. Mei and Kadri (2018), as summarised below:

$$x_0 = \frac{\left(\widehat{t}_2 - \widehat{t}_1\right)c}{\left\{1-\left[\frac{\pi c}{2h\widehat{\Omega}_{\widehat{t}_2}}\right]^2\right\}^{-1/2} - \left\{1-\left[\frac{\pi c}{2h\widehat{\Omega}_{\widehat{t}_1}}\right]^2\right\}^{-1/2}}; \tag{8}$$

$$t_0 = \widehat{t}_j - \frac{x_0}{c}\left\{1-\left[\frac{\pi c}{2h\widehat{\Omega}_{\widehat{t}_j}}\right]^2\right\}^{-1/2}; \quad y_0 = \sqrt{(t_0 c)^2 - x_0^2},$$

where $\widehat{\Omega}_j$ is the frequency calculated from the given pressure signal at a given point j, and $\widehat{t}_j$ is the corresponding time at the point.

Similarly, the orientation of the fault can be calculated by Eq. (8.4) of Ref. Mei and Kadri (2018), i.e. $\theta = 90^\circ - \tan^{-1}(x_0/y_0)$, which can be compared against tectonic plate boundaries and estimations made by seismic recordings analysis. Next, the dimensions of the fault, and the vertical uplift speed and duration are calculated as detailed below.

2.2.1. Width

The fault width ($2b$) modulates the pressure signal through $\sin(kb)$, as shown in Eq. (4). Hence, by selecting pressure points, that are in close proximity to the envelope, e.g. near pressure amplitude extrema from the signal wave packet, the width can be calculated from $\sin(kb) = 1$, see Fig. 2.

The wavenumber k is calculated using relation (7), which by substitution in $\sin(kb) = 1$, yields

$$b_m = \frac{\pi(m-1/2)c^2\widehat{t}_j}{\widehat{\Omega}_j x_0}, \quad m = 1, 2, 3\ldots, \tag{9}$$

that corresponds to a countable infinity of possible solutions for b. The process described in this subsection is repeated, using different points j from the signal, resulting in a probability density function composed by potential solutions that correspond to the different possible modes, where $m = [1-20]$ are considered. The solutions are analysed and averaged, leading to the most probable value $\overline{b}$ as illustrated in Fig. 3.

2.2.2. Duration

To find the duration of the event ($2T$), the ratio between two different pressure points i and j from the signal described by Eq. (4) is taken to reduce the number of unknowns:

$$\frac{\widehat{p}_i}{\widehat{p}_j} = \frac{|A_i|/\sqrt{k_i}}{|A_j|/\sqrt{k_j}} \frac{\sin\left(k_i\overline{b}\right)}{\sin\left(k_j\overline{b}\right)} \frac{\sin\left(\widehat{\Omega}_i T\right)}{\sin\left(\widehat{\Omega}_j T\right)}. \tag{10}$$

Eq. (10) is independent of W_0 and comprises two unknowns, T and L. The latter dictates the behaviour of the envelope A, which is nonlinear, as defined in Eq. (6).

There are infinitely many possible combinations of L and T that satisfy Eq. (10). We choose the most probable value ($\overline{T}$) that has the highest number of solutions within a given range, as illustrated in Fig. 4.

2.2.3. Uplift speed and length

Next, attention is focused on W_0 and L. Rewriting Eq. (4), W_0 can be expressed explicitly as

$$W_0 = \frac{\widehat{P}_j}{\rho|A_j|\frac{2^{7/2}c}{\sqrt{\pi^3 x_0 k_j}}\sin\left(k_j\overline{b}\right)\sin\left(\widehat{\Omega}_j\overline{T}\right)}, \tag{11}$$

where $|A_j|$ is the value of the envelope factor associated with the time $\widehat{t}_j$. Eq. (11) has two degrees of freedom, W_0 and L. Although, there are

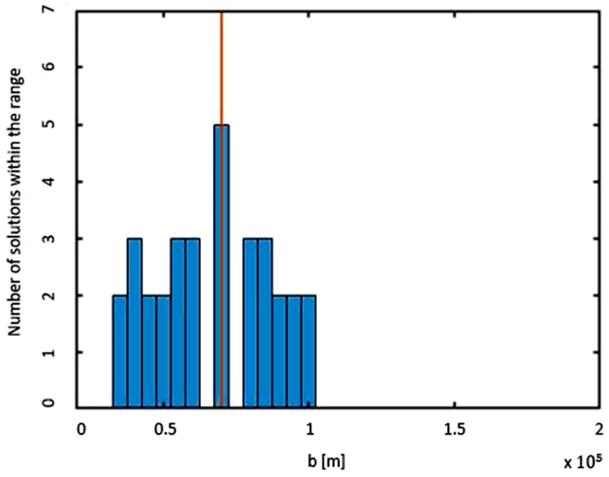

Fig. 3. Convergence diagram of solutions for the calculation of b. The wavenumbers k_j are associated with 5 different points in time along the signal. The average value of the half width $\overline{b}$ is 70 km; the red vertical line represents the actual solution.

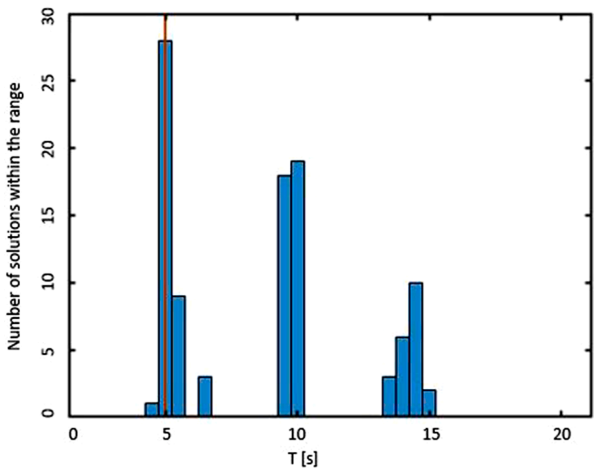

Fig. 4. Convergence diagram for the potential combinations of L and T that satisfy Eq. (10). The highest density of solutions is located around lines with the same value for T, therefore, the number of possible solutions for T is reduced to three in this case, where the final solution for half the duration is identified at $\overline{T} = 5$ s, i.e. full duration $2\overline{T} = 10$ s. The red vertical line represents the actual solution.

several potential W_0 solutions for each possible L that satisfy Eq. (11), the solutions can be constrained within ranges defined by previous documented effective earthquake dimensions, e.g. see Wells and Coppersmith (1994). For each combination of L and W_0, within the established ranges, a synthetic pressure envelope is generated by Eq. (4) and compared with the actual (recorded) pressure envelope of the signal. This procedure is done for two different inputs of k_j and $\widehat{\Omega}_j$ ($j = 1, 2$), leading to two three-dimensional surfaces, $S_1(L, W_0, err_1)$ and $S_2(L, W_0, err_2)$, where err_1 and err_2 are the absolute errors between the pressure generated by the potential combinations of W_0 and L and the actual pressure in the studied signal. Both surfaces reside in a three-dimensional space so that they intersect on a curve, which we average in both W_0 and L directions, producing a unique final solution for W_0 and L.

2.2.4. A note on the far-field solution

Stationary phase approximation was applied by Mei and Kadri (2018) in order to reach an analytical solution for the acoustic-gravity bottom pressure, enabling a near real-time analysis of the signal. Note that the far-field is at $x/h \gg 1$, however, due to the fact that, b is typically much larger than h, a few tens of kilometres away would already fall in the far-field of the mathematical solution, yet they are relatively in the near field of the fault. Table 1 of Kadri et al. (2017) shows an error of 10% at a distance of 50 km, which drops to 0.3% at a distance of 500 km.

3. Inverse model

We propose an inverse model that processes acoustic pressure signals and provides a probabilistic estimation of the fault geometry and dynamics in near real-time. The steps required to apply the model are described in this section in some detail for both synthetic and real hydrophone recordings.

3.1. Inverse model application: synthetic signals

A general flow chart of the inverse model process is presented in

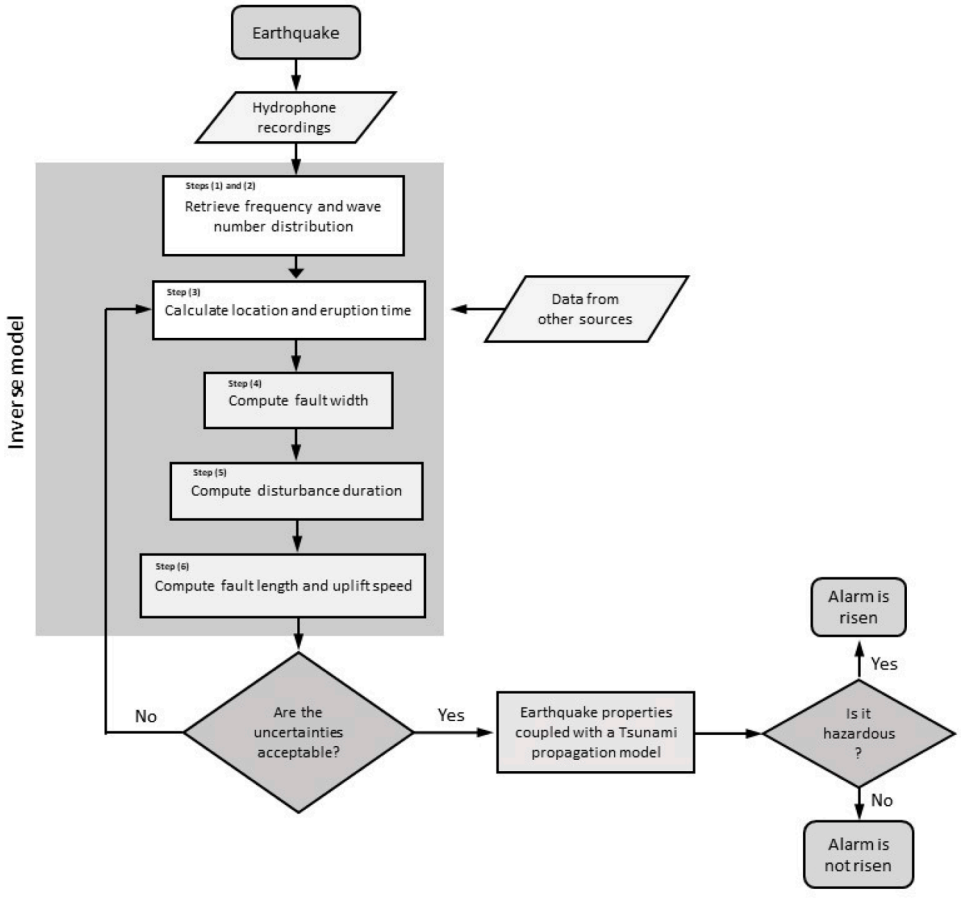

Fig. 5. Inverse model application flowchart - from acoustic pressure signal arrival to probabilistic calculation of source properties.

Fig. 5.

3.1.1. Steps 1 & 2: frequency and wavenumber distribution

The first step, prior to analysing the pressure signal, is to identify regions composed by points that are likely to lead to minimum errors in the solution, see Fig. 6. Subsequently, we calculate the frequency distribution; time differences between five consecutive peaks from the signal, $j-2$, $j-1$, j, $j+1$ and $j+2$, are obtained and the weighted average is computed, leading to the period associated to j, see Fig. 7. The weighted average is defined by

$$\widehat{T}_{\widehat{t}_j} = \frac{c_1\widehat{T}_1 + c_2\widehat{T}_2 + c_3\widehat{T}_3 + c_4\widehat{T}_4}{c_1 + c_2 + c_3 + c_4}, \tag{12}$$

where $\widehat{T}_{\widehat{t}_j}$ is the period associated with a time point $\widehat{t}_j$, the remaining parameters in Eq. (12) are defined by:

$$\widehat{T}_m = \widehat{t}_{j+m-3} - \widehat{t}_{j+m-2}, \quad c_m = \frac{\widehat{T}_m}{\widehat{T}_1 + \widehat{T}_2 + \widehat{T}_3 + \widehat{T}_4}, \quad m = 1,2,3,4 \tag{13}$$

where $\widehat{T}_1 < \widehat{T}_2 < \widehat{T}_3 < \widehat{T}_4$ and c_1, c_2, c_3, c_4 are the weighting coefficients.

In Fig. 6, Eqs. (12) and (13) are computed for every identified pressure peak in the signal and the associated frequency distribution is calculated by applying $\widehat{\Omega}_{\widehat{t}_j} = 2\pi/\widehat{T}_{\widehat{t}_j}$. Errors retrieving the frequency distribution are minimised if points that fall near pressure amplitude extrema are selected, see Fig. 7. The highlighted regions in Fig. 6 comprise points with associated small errors,

$$err_{\widehat{\Omega}_{\widehat{t}_j}} = \frac{|\widehat{\Omega}_{\widehat{t}_j} - \Omega_{\widehat{t}_j}|}{\Omega_{\widehat{t}_j}} 100[\%]. \tag{14}$$

3.1.2. Step 3: location and eruption time

Eq. (8) is sensitive to errors in frequency measurement, in particular, when selecting two pressure points that lie in close proximity to each other. Consequently, the denominator of Eq. (8) tends to zero, which increases the instability of the solution and induces larger errors - see highlighted areas on Fig. 8. Therefore, these scenarios are avoided by the model.

Although, differences in pressure between the peaks in the signal and the corresponding points that lie on the actual envelope can induce uncertainties in the results, errors in the frequency are found to be more significant, as demonstrated in Section 4. With these observations in hand, the frequency distribution, fault location, and eruption time are calculated and used to compute the wavenumber distribution by Eq. (9).

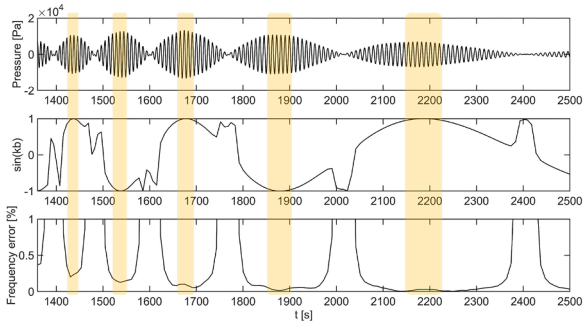

Fig. 6. Top: Synthetic pressure signal at the relative location $x_0 = 1500$ km, $y_0 = 500$ km induced by a slender fault, where $L = 700$ km, $b = 140$ km, $W_0 = 0.1$ m/s and $T = 10$ s, the average sea depth is $h = 4$ km. Middle: Distribution of $sin(k_j b)$ along the signal. Bottom: Errors in frequency calculation by Eq. (14). The highlighted regions correspond to areas related to low errors due to the pressure points being close to the envelope and meeting the condition $sin(kb) = 1$.

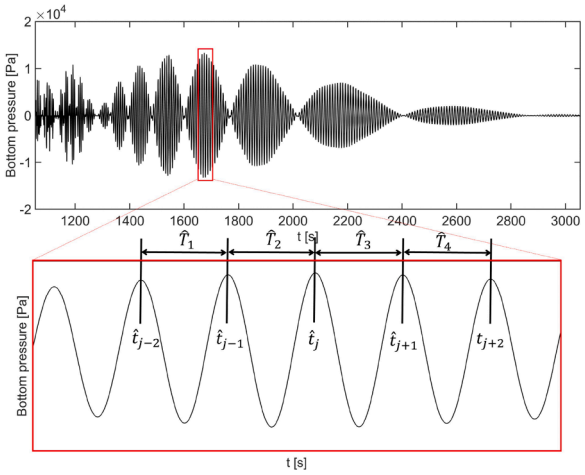

Fig. 7. Above: Pressure time series induced by vertical slender fault motion. Below: Closer look to the region where consecutive peaks are used to calculate the period related to the central peak, $\widehat{T}_{\widehat{t}_j}$.

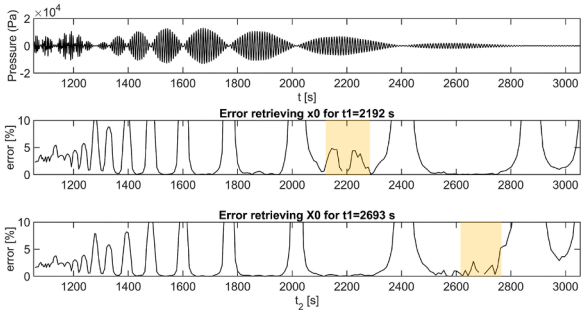

Fig. 8. Top: Synthetic pressure signal. Middle and Bottom: Eq. (8) is solved for a fixed t_1 and every possible t_2 along the signal. The error is calculated by comparing the calculated x_0 with the actual solution. Two different scenarios for t_1 from the same signal are shown. t_1 lies in the coloured areas, demonstrating that points in close proximity induce unnecessary errors in the solution.

3.1.3. Step 4: fault width

The model selects regions in the signal associated to minimum uncertainties, as previously described. The closer these regions to the envelope, the more accurate the approximation $\sin(kb) = 1$ becomes, see Fig. 2. The wavenumber (k) is obtained by using the retrieved frequencies in Eq. (7). Then, Eq. (9) is used for each selected pressure point and its associated wavenumber (k) with a predefined number (n) of solutions. This leads to several sets of n solutions that are constrained in ranges based on estimations of effective earthquake surface fault widths by Wells and Coppersmith (1994). The model analyses the local density of solutions by generating a grid with a fixed step, identifying the step containing the highest number of solutions and selecting it as the weighted average solution for the half width (b), see Fig. 3.

3.1.4. Step 5: disturbance duration

Eq. (10) has two unknowns, T and L. Thus, these can be solved numerically by selecting two sets of points, each comprising two pressure points, $\widehat{p}_i$ and $\widehat{p}_j$, two frequencies $\widehat{\Omega}_i$ and $\widehat{\Omega}_j$, and two wavenumbers k_i and k_j. Each solution of, say L, leads to an infinite number of solutions for T. However, we limit the solution to realistic ranges associated with the specific region, e.g. $L = [10,900]$ km (Wells and Coppersmith, 1994), and $T = [3,20]$ s (Decker et al., 1992; Ekström et al., 2012). This leads to a two-dimensional matrix containing possible combinations of L and T, that satisfy Eq. (10).

The periodic nature of Eq. (10) leads to a periodic distribution of

solutions for T. A probability density function for the number of solutions within a given range is established. Pairs of points i,j are considered as needed until convergence of the possible solution is reached, see Fig. 4. We consider all possible duration T_c that are associated with high convergence of solutions around them, such that $T_c \geq \alpha T_{max}$, where $T_{\max}$ is duration with highest number of solutions, and α is an arbitrary fraction, e.g. $\alpha = 0.6$ is found efficient in terms of computation time and number of solutions. Eq. (10) is computed for all the considered solutions of T and all possible solutions for L. For each chosen T, the number of combinations with L that satisfy Eq. (10) are analysed and the duration with highest number of solutions is selected as the converged value for half the uplift duration.

3.1.5. Step 6: length and uplift speed

The last two unknown parameters to be retrieved are L and W_0. To address this challenge, several combinations of W_0 and L are chosen in regular intervals within realistic ranges. Pressure envelopes, with low sampling frequency (to reduce CPU time), are generated for each combination of L and W_0 using Eq. (10). The generated pressure envelopes and the corresponding pressure points from the signal are compared against each other, so the average difference in pressure is given by

$$E_a = \frac{1}{N_{peak}} \left\{ \sum_{n=1}^{N_{peak}} \frac{|p_{env} - \widehat{p}_{peak_n}|}{\widehat{p}_{peak_n}} \right\} \tag{15}$$

where N_{peak} is the number of chosen peaks used, p_{env} is the pressure point on the envelope, $\widehat{p}_{peak_n}$ is the measured pressure of each of the chosen peaks. By minimizing E_a, two combinations of W_0 and L, that correspond to the minimum average pressure differences obtained using Eq. (15), are chosen and their arithmetic mean is calculated, and thus L_c is obtained.

Considering that the solution for L has some degree of uncertainty, in order to calculate the last parameter W_0 five different values for the length are considered and Eq. (11) is calculated for each one of them: $L_1 = L_c - (0.1L_c)$; $L_2 = L_c - (0.05L_c)$; $L_3 = L_c$; $L_4 = L_c + (0.1L_c)$; $L_5 = L_c + (0.05L_c)$. This procedure leads to five solutions for W_0, that can be arithmetically averaged, in order to achieve mean solution for the uplift speed. The choice of five L values about L_c is arbitrary, and more values can be considered, though the CPU time can increase substantially.

3.2. Inverse model application: real hydrophone recordings

Waves induced by the tectonic event are firstly detected by seismometers (P-waves), which can shed light on the epicentre location and magnitude of the event, thus, the mentioned data can be used to reduce the uncertainties associated to the inverse model results.

As demonstrated in detail in the Section 5, the inverse model can provide an estimation of the source characteristics when applied to hydrophone recordings. Here, we focus on the application to real scenarios side of the model, which requires additional steps due to the presence of noise and signal distortion of the real data. In particular, attention is focused on time-pressure series of acoustic signals recorded in the Cascadia Basin by a hydrophone of Ocean Networks Canada (Archive, 2020), after a 6.9 M_w earthquake in the southern East Pacific ridge on October 9th 2014, see Fig. 9.

3.2.1. Step 1: potential location of the source

Initially, the frequency distribution of the leading mode is calculated, which is a function of time (t, relative to the eruption time t_0), depth (h), and orientation of fault (x_0 and y_0), see Eq. (7). The total distance between the hydrophone and the earthquake is approximately 9000 km, which can be given by various combinations of x_0 and y_0, i.e. different possible orientations. The potential coordinates are constructed as two vectors: the first comprises the possible solutions for x_0, ranging from 0 to 9000 km on regular intervals of 50 km; and the second has the solutions y_0 corresponding to the possible x_0 in the first vector. Eq. (7) is computed for each possible coordinate (x_0, y_0) that lead to frequency distributions with minimum value higher than the minimum frequency threshold. The lower limit of the signal frequencies in the power spectrum is identified, in this case at 3 Hz. This procedure leads to only five potential solutions for the location of the earthquake in the presented case, $x_{0,1} = 8750$ km and $y_{0,1} = 2100$ km, $x_{0,2} = 8800$ km and $y_{0,2} = 1887$ km, $x_{0,3} = 8850$ km and $y_{0,3} = 1636$ km, $x_{0,4} = 8900$ km and $y_{0,4} = 1337$ km, $x_{0,5} = 8950$ km and $y_{0,5} = 947$ km. A comparison between the spectrogram and the potential frequency distributions is made in Fig. 10.

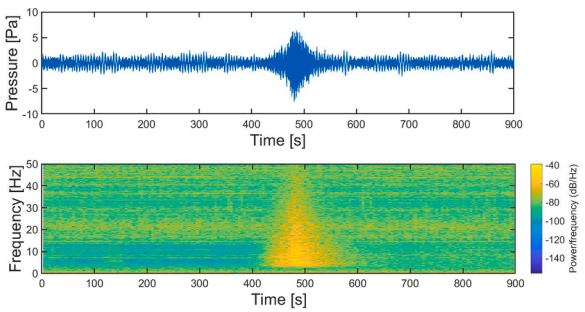

Fig. 9. Top: Calibrated pressure signal, induced by a 6.9 M_w earthquake recorded by a icListen LF 224. Bottom: Corresponding spectrogram.

3.2.2. Step 2: Signal detection

To identify the beginning of the relevant signal content, the short-time energy distribution is calculated using $\sum_{j=1}^{J} |p_j|^2$, where p_j is the pressure amplitude of the jth sample and J is the sample size. Here we consider a sample size of $J = 4000$. The threshold for the identification of the signal disturbance is set at 1.2 times the average value of the short-time energy distribution for the first ten seconds in the recorded time series, see in Fig. 11.

3.2.3. Step 3: envelope tracking

In order to minimise the deviation between selected pressure points at the actual signal and the corresponding approximated points at the envelope, we seek points at the vicinity of the extrema. Thus, applying an iterative identification method of local maxima (or minima), the total difference between selected pressure points and the theoretical envelope is reduced. The method is repeatedly applied until the relation $2\pi/T_{peaks}$ is verified to lie below the previously obtained theoretical frequency distributions for the first mode for all the identified peaks, where T_{peaks} are the averaged times between consecutive peaks. This is a necessary condition in order to associate the computed ideal frequency distributions to the identified local maxima in the pressure signal.

Each identified pressure point is associated to a frequency point of each of the potential first mode frequency distributions, see Fig. 12.

3.2.4. Step 4: estimation of characteristics range

Wells and Coppersmith (1994) established correlations between

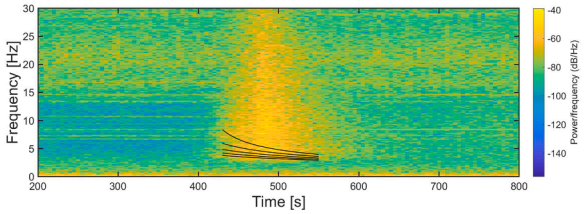

Fig. 10. Spectrogram associated to the studied pressure signal. The black lines represent the five possible synthetic ideal distributions of the first acoustic mode.

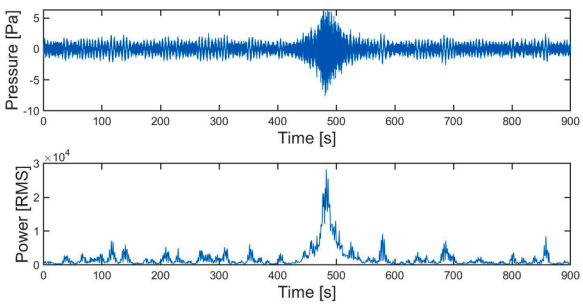

Fig. 11. Above: Acoustic disturbance originated by the studied tectonic event. Below: Short-time energy distribution.

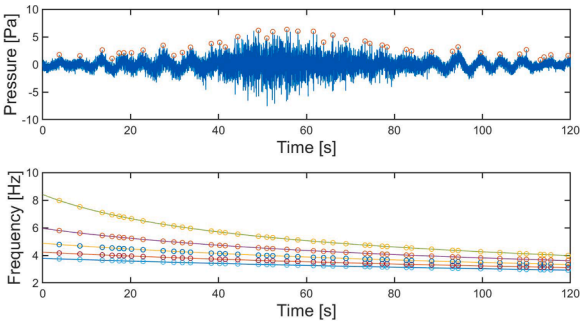

Fig. 12. Above: Acoustic signal. The identified pressure maxima are highlighted. Below: Five potential first mode frequency distributions for the signal. The points related to the highlighted maxima are circled.

magnitude, surface rupture length, width and ground displacement. Using these correlations an earthquake, say of magnitude M_w=6.9, is associated with length $2L \approx 35$ km (Fig. 9 in Wells and Coppersmith, 1994) and area $A \approx 620$ km^2 (figure 16 in Wells and Coppersmith, 1994), thus the width (in case of a rectangle) is $2b \approx 17.71$ km. An estimation of the average vertical displacement is $d \approx 0.75$ m (Fig. 11 in Wells and Coppersmith, 1994). It is worth mentioning that the used correlations are based on empirical values which include significant scatter (Wells and Coppersmith, 1994). Using these correlations (and scattering) we establish reasonable ranges for the earthquake characteristics for the analysed earthquake, e.g. see ranges listed in Table 1.

3.2.5. Step 5: calculation of the source characteristics

Steps 4–6 of the inverse model applied to the theoretical scenarios (Section 3.1) are applied to each potential frequency distribution of the first acoustic mode and the associated pressure points from the signal. As a result, we obtain 30 sets of solutions for every frequency distribution, which leads to a total of 150 solutions for each fault characteristic. The distribution of the four fault characteristics are shown in the histograms in Fig. 13.

4. Sensitivity analysis

Since the proposed model requires approximating the selected pressure amplitudes, and the associated frequencies, it is important to evaluate the deviation that small errors in the approximations may lead to. In particular, the model is tested using synthetic data with different levels of noise and errors. For the sake of brevity, the results related to this analysis are graphically displayed in Appendix A. Two main sources of error are identified in the results: (1) frequency calculation; and (2) envelope tracking (assumption of $\sin(kb) = 1$). Additionally, errors can be related to difference between the points in the pressure signal used as input to the model and the corresponding points on the theoretical envelope. Nevertheless, this type of uncertainties can be minimised by selecting pressure points associated to local maxima as mentioned above.

To proceed with the analysis, a theoretical case scenario is generated, see Table 2. Initially, sensitivity to errors in frequency calculation of Eq. (8) is tested by introducing random errors up to a maximum level of 100% of the calculated frequency distribution, see Figs. A.15 and A.16. In this case, the relative location of the slender fault shows high sensitivity to errors, especially, the solution for y_0, see Figs. A.15 and A.16. Practically, the location is not an issue as it normally obtained with high accuracy using seismometers. Thus, in practice, input data from seismometers can be used to tune the parameters leading to y_0.

For the rest of the eruption characteristics, three configurations for the number of points used to compute each set of solutions are tested. The first configuration consists of the initially selected points (one set) only; the second configuration considers two additional sets of points

Table 2
Theoretical slender fault properties used for the sensitivity analysis.

x_0[km]	y_0[km]	$2b$[km]	$2T$[s]	$2L$[km]	W_0[m/s]
1000	500	160	10	1600	0.100

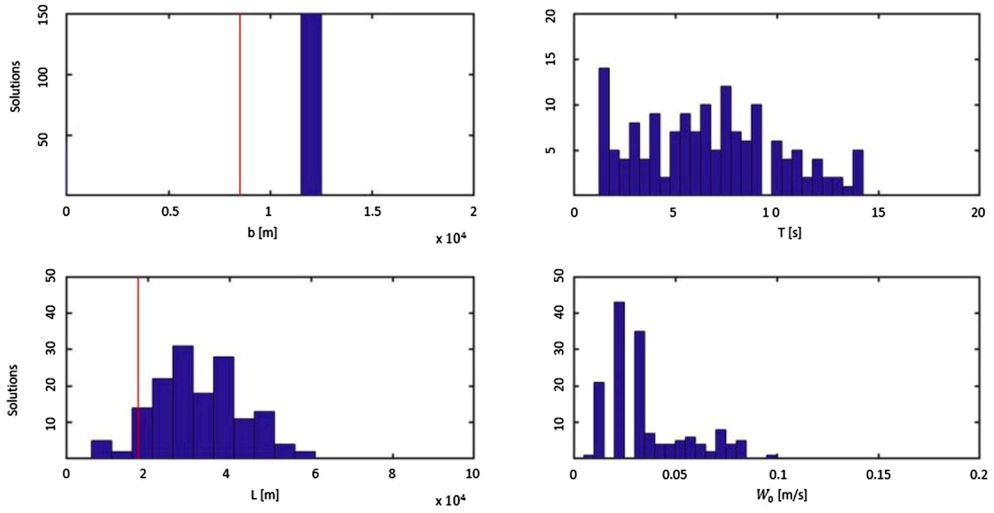

Fig. 13. Histograms of calculated solutions for the half width, half duration, half length and uplift speed of the source. The average values are: $\overline{b} = 12.000$ km, $\overline{T} = 6.396$ s, $\overline{L} = 24.873$ km and $\overline{W_0} = 0.049$ m/s. The vertical red lines indicate the estimated characteristics by the relations found in Wells and Coppersmith (1994).

(three sets in total), where an extra point is located at each side of the point initially selected in the first configuration; the third configuration includes four additional sets of points (5 sets in total), considering two extra points at each side of points selected in the first configuration.

The application of the model to each set of points results in a set of solutions, that are averaged, to finally give a probability density of the property. The number of chosen points used to compute each set of solutions is analysed. A range of two points, which is the minimum, up to eight points is considered. Note that, more points are not considered in the analysis as the computations become extensive. Errors in location calculations (x_0, y_0) are assumed to be under 5%, which is a reasonable assumption considering that data from seismometers are at hand. Random errors in frequency and pressure amplitude are introduced independently to evaluate their independent influence on the solutions. It is remarkable that choosing five points to calculate each set of characteristics, and using three sets of points, provides a good balance between computational efficiency and accuracy, see Figs. A.17–A.21.

Next, the number of points chosen to compute each set of solutions is fixed to five, and ten sets of solutions are obtained and averaged, leading to a final solution for each characteristic. Then, different levels of random errors in pressure and frequency measurements are introduced and the model is applied 30 times for each synthetic noise scenario. It appears that errors in frequency induce a higher variance in the solutions obtained by the model, which results in higher uncertainties - see Figs. A.22 and A.23.

The CPU times required by the model increase (almost) linearly with the number of solutions demanded by the user (Fig. 14). Moreover, the computational effort is related to the size of the ranges chosen to constrain the potential solutions used as input to the model.

5. Results

5.1. Analysis of synthetic data

In theory, in order to estimate the slender fault geometry and dynamics only a few points are required from the signal. Nevertheless, the large amount of points (and combination of points) that can be applied, leads to a probability density of solutions. This allows applying the inverse model in scenarios with noise and distorted pressure signal.

The model has been tested using synthetic signals generated by Eq. (10) under different input configurations in order to quantify its accuracy and computational efficiency along its response to induced Gaussian noise. Different model parameters have been considered, such as the amount of sets of points and the quantity of points used to compute each set of characteristics. The choice of five points with two additional sets of points to compute each set of solutions, as shown in Section 4, leads to an acceptable relation between model accuracy and computational effort. Thus, the set-up parameters can be configured to minimise the uncertainties associated to the solutions.

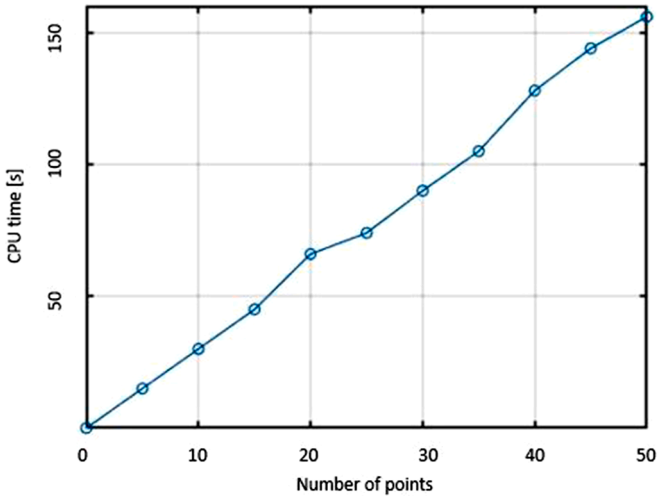

Fig. 14. CPU times for different amounts of points used to compute each set of solutions requesting five sets of solutions. The processor used is Intel(R) Core (TM) i5-4690 CPU, speed [3.5 GHz-3.5 GHz] and 8 GB RAM.

Three synthetic cases, based on real earthquakes, are generated. Case A: 11 March 2011, 9.1 M_w Tohoku earthquake. Case B: 26 December 2004, 9.1 M_w Sumatra earthquake. Case C: 22 May 1960, 9.5 M_w Chile earthquake. Note that even though the synthetic cases presented here are based on real earthquakes, the main target is to generate numerical scenarios to study the behaviour of the inverse model, hence some properties may deviate from real ones. The eruption duration in cases A and B is obtained from the Global CMT catalog (Decker et al., 1992; Ekström et al., 2012), the duration in case C is chosen to be in the same order of magnitude as cases A and B. The simplified geometric properties (length and width) of the effective slender faults are based on previous research related to the mentioned tectonic events. In case A, rupture length and width of 440 km and 180 km were reported (Yagi and Fukahata, 2011), respectively. The rupture length in case B was estimated to be over 1000 km and the width between 120 and 140 km (Gahalaut et al., 2006). Case C has a 800 km rupture length and 200 km width (Kanamori and Cipar, 1974). The rest of the properties were estimated using scaling relations found in Wells and Coppersmith (1994), see Table 3.

5.2. Analysis of real data

We consider an earthquake on 9th October 2014, $M_w = 6.9$, which was detected on the southern East Pacific ridge. The magnitude, centroid time, depth of the hypocentre, half duration and location of the event are reported in the Global CMT catalog (Decker et al., 1992; Ekström et al., 2012). The tectonic event occurred at 2:14:42.4 UTC at the coordinates 32.34 S and 110.81 W, the depth of the hypocentre was 12 km and the half duration 7.3 s. The angles of the fault planes are 90° and 296° Strike; 39° and 54° Dip; and 69° and 106° Slip, which suggests that, the earthquake had an effective vertical motion component. The earthquake triggered a tsunami that was recorded on Easter Island region with a maximum amplitude of 47 cm (NOAA, 2015).

The hydrophone data was provided by Canada Ocean Network (Archive, 2020); the recording hydrophone is type icListen LF 224 (sampling frequency 4 kHz), deployed in the Cascadia Basin (47.76 N and 127.75 W) at a depth of 2662 m. The distance between the epicentre of the earthquake and the hydrophone is approximately 9000 km, resulting in 100 min of travel time for the acoustic radiation, at a constant speed of $c = 1500$ m/s. The hydrophone recordings, shown in Fig. 9, start at 03:48:2.3 UTC and the pressure disturbance, induced by the above described earthquake, is identified approximately at 03:55:0 UTC, matching the expected travel time (100 min).

The pressure signal, displayed in Figs. 9 and 11, is calibrated using the sensitivity file provided by Canada Ocean Network for the corresponding hydrophone. (the provided signal was initially calibrated between 1 and 1600 Hz).

The model delivered a unique solution for b, due to the fact that, ideal frequency distributions without noise are assumed, see Section 3.2. On the other hand, the solutions for T and L are distributed symmetrically around the mean, see in Fig. 13, whereas the distribution of solutions for W_0 presents positive skewness. The calculated values of b, L, and vertical displacement, are in the same order of magnitude as the values based on (Wells and Coppersmith, 1994), see Fig. 13. The calculated duration of the vertical uplift ($2\overline{T} = 13.9$ s) is in agreement with the duration provided by the Global CMT (14.6 s, see Table 4).

Table 3
Comparison between input parameters used to generate synthetic pressure signals and retrieved inverse process parameters. The computational effort needed by the model to calculate 30 sets of solutions using 5 points to compute each set with a PC of characteristics, processor Intel(R) Core(TM) i5-4690 CPU, speed [3.5 GHz-3.5 GHz] and 8 GB RAM is reported.

Case		x_0 [km]	y_0 [km]	b [km]	T [s]	L [km]	W_0 [m/s]	CPU [s]
A	Input	1000	300	80.0	35.0	250	0.100	183
	Retrieved	998	283	76.5	28.7	316	0.069	
B	Input	800	100	70.0	45.0	750	0.100	126
	Retrieved	796	100	70.1	49.5	681	0.138	
C	Input	1500	500	100	30.0	400	0.100	171
	Retrieved	1464	464	96.5	34.3	471	0.072	

Table 4
Comparison between the calculated effective earthquake properties by the inverse model and the estimated properties by relations found in Wells and Coppersmith (1994).

Property	Inverse model	Wells and Coppersmith (1994)
Length ($2L$) [km]	49.7	35.0
Area [km^2]	1193	620
Width ($2b$) [km]	24.0	17.7
Vertical displacement [m]	0.626	0.750

6. Discussion and conclusions

Some simplifications were assumed by Mei and Kadri (2018) to derive an analytical solution for the generation and propagation of acoustic radiation by an uplifting slender fault. The assumption of a rectangular slender fault may correspond to many earthquakes, though we employ that as a mechanism for the generation of an *effective* water uplift rather than an actual description of the full complex dynamics of the rupture. Hence, one could argue that any earthquake that generates a tsunami can be associated with an effective vertical uplift of the water volume. Noting that the leading acoustic mode lengthscale is much longer than the water depth, the assumption of a flat rigid seabed is justified as long as the water depth is above some critical value (Williams et al., 2021); below it the interaction with the elastic bottom becomes relevant. In addition, the effect of sound speed variations is minor, as the relevant leading acoustic mode has an extremely low frequency (Jensen et al., 2011) and the whole ocean column acts as a guideline. The vertical uplift speed is assumed to be constant, which is unlikely to be the case in actual scenarios. However, the more realistic uplift with acceleration may modify the absolute amplitudes in the signal (acceleration will increase the amplitude, whereas deceleration will decrease it) but not the ratios which is what the inverse model applies.

In the analysis carried out in this study, attention was focused on theoretical scenarios based on real earthquakes, and sensitivity of the calculated parameters to uncertainties in the signal, say due to ambient noise. The evaluation of data with noise may require implementing various techniques (such as cross-correlation between several hydrophones if applicable) to identify the relevant signal more accurately. Therefore, we anticipate an improvement of the performance of the proposed inverse model as further filtering techniques are employed.

Including gravity effects may only slightly modify the dispersion properties of the leading (low frequency) acoustic modes. However, once gravity is included, retrieving the fault properties will directly result in the solution for the tsunami, hence minimising tsunami model calculation time. Another aspect that needs to be included in future studies is the elasticity of the sea floor, in particular near critical depths, where leading acoustic modes couple with the elastic floor boosting its propagation speed to near the speed of sound in the elastic layer, typically over 3000 m/s (Eyov et al., 2013; Nosov and Kolesov, 2007). This becomes important when analysing transects with large variations in water depths, or during shoaling and upon interaction with shelf-breaks.

The proposed model is linear, therefore, complex earthquake geometries can be described by multi-fault scenarios, consisting on several single faults that can be triggered independently (Hamling et al., 2017), and in turn each fault can be divided into segments following the rupture propagation. Non-linear aspects may become important when analysing propagation over large distances and random topography.

CRediT authorship contribution statement

Bernabe Gomez: Formal analysis, Investigation, Methodology, Writing - review & editing. **Usama Kadri:** Conceptualization, Formal analysis, Methodology, Supervision, Writing - review & editing.

Declaration of Competing Interest

The authors declare that they have no known competing financial interests or personal relationships that could have appeared to influence the work reported in this paper.

Acknowledgements

The authors are grateful to Canada Ocean Networks for providing Open Source hydrophone data. This work has been supported by the Engineering and Physical Sciences Research Council EP/N509449/1.

Supplementary material

Supplementary material associated with this article can be found, in the online version, at 10.1016/j.apor.2021.102557

References

Abdolali, A., Kadri, U., Kirby, J.T., 2019. Effect of water compressibility, sea-floor elasticity, and field gravitational potential on tsunami phase speed. Sci. Rep. 9 (1), 1–8.
Archive, O.N.C.D., 2020. Hydrophone data from 03:48 utc 2014/09/10 to 04:03 utc 2014/09/10, oceans networks Canada, university of Victoria, Canada. downloaded on september 2019.http://www.oceannetworks.ca.
Bilek, S.L., Lay, T., 1999. Rigidity variations with depth along interplate megathrust faults in subduction zones. Nature 400 (6743), 443.
Cecioni, C., Bellotti, G., 2018. On the resonant behavior of a weakly compressible water layer during tsunamigenic earthquakes. Pure Appl. Geophys. 175 (4), 1355–1361.
Decker, K., Hirata, K., Groudev, P., 1992. Guidance document on practices to model and implement earthquake. Bull. Seism. Soc. Am 96, 2181–2205.
Ekström, G., Nettles, M., Dziewoński, A., 2012. The global CMT project 2004–2010: centroid-moment tensors for 13,017 earthquakes. Phys. Earth Planet. Inter. 200, 1–9.
Eyov, E., Klar, A., Kadri, U., Stiassnie, M., 2013. Progressive waves in a compressible-ocean with an elastic bottom. Wave Motion 50 (5), 929–939.
Fujii, Y., Satake, K., 2007. Tsunami source of the 2004 Sumatra–Andaman earthquake inferred from tide gauge and satellite data. Bull. Seismol. Soc. Am. 97 (1A), S192–S207.
Gahalaut, V., Nagarajan, B., Catherine, J., Kumar, S., 2006. Constraints on 2004 Sumatra–Andaman earthquake rupture from GPS measurements in andaman–nicobar islands. Earth Planet. Sci. Lett. 242 (3-4), 365–374.
Hamling, I.J., Hreinsdóttir, S., Clark, K., Elliott, J., Liang, C., Fielding, E., Litchfield, N., Villamor, P., Wallace, L., Wright, T.J., et al., 2017. Complex multifault rupture during the 2016 mw 7.8 Kaikōura earthquake, New Zealand. Science 356 (6334), eaam7194.
Hendin, G., Stiassnie, M., 2013. Tsunami and acoustic-gravity waves in water of constant depth. Phys. Fluids 25 (8), 086103.

Jensen, F.B., Kuperman, W.A., Porter, M.B., Schmidt, H., 2011. Computational Ocean Acoustics. Springer Science & Business Media.
Kadri, U., Crivelli, D., Parsons, W., Colbourne, B., Ryan, A., 2017. Rewinding the waves: tracking underwater signals to their source. Sci. Rep. 7 (1), 13949.
Kadri, U., Stiassnie, M., 2012. Acoustic-gravity waves interacting with the shelf break. J. Geophys. Res. 117 (C3).
Kanamori, H., Cipar, J.J., 1974. Focal process of the great chilean earthquake may 22, 1960. Phys. Earth Planet. Interiors 9 (2), 128–136.
Krüger, F., Ohrnberger, M., 2005. Tracking the rupture of the m w = 9.3 Sumatra earthquake over 1,150 km at teleseismic distance. Nature 435 (7044), 937.
Maksymowicz, A., Chadwell, C., Ruiz, J., Tréhu, A., Contreras-Reyes, E., Weinrebe, W., Díaz-Naveas, J., Gibson, J., Lonsdale, P., Tryon, M., 2017. Coseismic seafloor deformation in the trench region during the mw 8.8 maule megathrust earthquake. Sci. Rep. 7, 45918.
Mei, C.C., Kadri, U., 2018. Sound signals of tsunamis from a slender fault. J. Fluid Mech. 836, 352–373.
Moreno, M.S., Bolte, J., Klotz, J., Melnick, D., 2009. Impact of megathrust geometry on inversion of coseismic slip from geodetic data: application to the 1960 chile earthquake. Geophys. Res. Lett. 36 (L16310) https://doi.org/10.1029/2009GL039276.
NOAA, 2015. National geophysical data center/world data service (ngdc/wds): Global historical tsunami database.
Nosov, M., 1999. Tsunami generation in compressible ocean. Phys. Chem. Earth Part B 24 (5), 437–441.
Nosov, M., Kolesov, S., 2007. Elastic oscillations of water column in the 2003 Tokachi-Oki tsunami source: in-situ measurements and 3-D numerical modelling. Nat. Hazards Earth Syst. Sci. 7 (2), 243–249.
Okal, E.A., 2001. T-phase stations for the international monitoring system of the comprehensive nuclear-test ban treaty: a global perspective. Seismol. Res. Lett. 72 (2), 186–196.
Okal, E.A., Talandier, J., Reymond, D., 2007. Quantification of hydrophone records of the 2004 Sumatra tsunami. Pure Appl. Geophys. 164 (2-3), 309–323.
Stiassnie, M., 2010. Tsunamis and acoustic-gravity waves from underwater earthquakes. J. Eng. Math. 67 (1-2), 23–32.
Wells, D.L., Coppersmith, K.J., 1994. New empirical relationships among magnitude, rupture length, rupture width, rupture area, and surface displacement. Bull. Seismol. Soc. Am. 84 (4), 974–1002.
Yagi, Y., Fukahata, Y., 2011. Rupture process of the 2011 Tohoku-Oki earthquake and absolute elastic strain release. Geophys. Res. Lett. 38 (L19307) https://doi.org/10.1029/2011GL048701.
Yamamoto, T., 1982. Gravity waves and acoustic waves generated by submarine earthquakes. Int. J. Soil Dyn. Earthq. Eng. 1 (2), 75–82.
Williams, Byron, Kadri, Usama, Abdolali, Ali, 2021. Acoustic–gravity waves from multi-fault rupture. Journal of Fluid Mechanics. https://doi.org/10.1017/jfm.2021.101. In press.